

Generative Spatiotemporal Data Augmentation

Jinfan Zhou^{*1,2} Lixin Luo^{*2} Sungmin Eum³ Heesung Kwon³ Jeong Joon Park²

¹University of Chicago ²University of Michigan, Ann Arbor ³DEVCOM Army Research Laboratory

zjf@uchicago.edu {lixinluo, jjparkcv}@umich.edu {sungmin.eum, heesung.kwon}.civ@army.mil

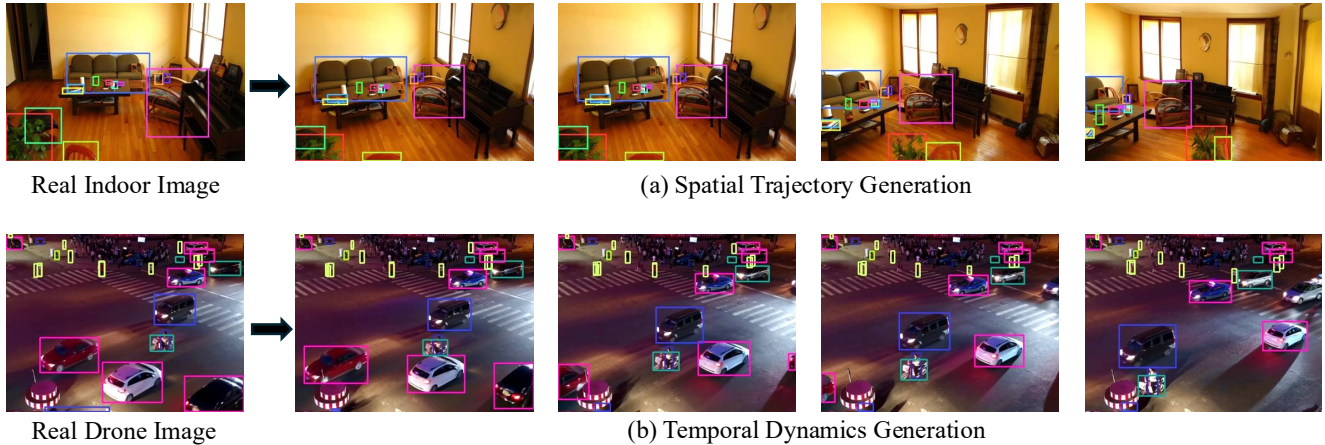


Figure 1. **Spatiotemporal augmentation from a single image.** Given a single real image (left), our method generates diverse spatial viewpoints (top row) and plausible temporal dynamics (bottom row) using video diffusion models. Bounding boxes are automatically propagated to all synthetic frames, enabling training with rich geometric and motion variation without additional manual annotation cost.

Abstract

We explore spatiotemporal data augmentation using video foundation models to diversify both camera viewpoints and scene dynamics. Unlike existing approaches based on simple geometric transforms or appearance perturbations, our method leverages off-the-shelf video diffusion models to generate realistic 3D spatial and temporal variations from a given image dataset. Incorporating these synthesized video clips as supplemental training data yields consistent performance gains in low-data settings, such as UAV-captured imagery where annotations are scarce. Beyond empirical improvements, we provide practical guidelines for (i) choosing an appropriate spatiotemporal generative setup, (ii) transferring annotations to synthetic frames, and (iii) addressing disocclusion—regions newly revealed and unlabeled in generated views. Experiments on COCO subsets and UAV-captured datasets show that, when applied judiciously, spatiotemporal augmentation broadens the data distribution along axes underrepresented by traditional and prior generative methods, offering an effective lever for improving model performance in data-scarce regimes.

*Equal contribution.

1. Introduction

Deep learning has driven remarkable progress in core vision tasks such as image classification [11, 20, 28], object detection [7, 15, 31, 39], and semantic segmentation [8, 27, 41]. However, this progress relies on large, diverse, and densely annotated datasets [10, 32, 44]. Collecting new viewpoints, camera motions, and object dynamics—especially in domains like drones, robotics, or long-tail scenes—often requires specialized hardware or repeated deployments, and manual annotation remains labor-intensive.

These challenges have motivated the use of generative models [16, 22, 36] to synthesize training data. Diffusion models now produce photorealistic images [40], 3D assets [37], and high-quality videos [5]. Yet despite this fidelity, prior work largely focuses on appearance-level augmentation, leaving open the question of how to leverage generative models to meaningfully expand a dataset’s spatiotemporal diversity.

In this work, we show that modern video diffusion models encode strong, implicit 3D and dynamic priors [18, 47, 56, 62] that can be directly exploited for perception. From a single input image, these models generate novel viewpoints and plausible temporal variations, yielding data with richer geometric and temporal coverage than the original dataset.

Because the frames are temporally coherent, visual foundation models [27, 38] can propagate annotations reliably across the generated sequence.

Our key idea is to demonstrate that an off-the-shelf video diffusion model acts as a powerful spatiotemporal data augmentation engine for object detection. We further provide practical guidelines, backed by extensive experiments, for how to use this augmentation effectively. This approach yields significant gains in data-scarce detection regimes: +3.8 mAP on a COCO [32] sub-dataset, +2.8 mAP on Vis-Drone [6], and +5.9 mAP on Semantic Drone [9]. To enable scalable deployment, we introduce an automated annotation pipeline that transfers bounding boxes across generated views, handles disocclusions, and offers tools for balancing coverage and fidelity. Our contributions are:

1. A first demonstration that an off-the-shelf video diffusion model can generate synthetic data that measurably improves object detection performance.
2. A fully automated annotation-transfer pipeline that leverages temporal consistency to produce accurate bounding boxes for all generated frames.
3. Extensive experiments offering guidelines on choosing video diffusion types, number of frames, disocclusion handling, camera trajectories, and other factors that influence the effectiveness of spatiotemporal augmentation.

2. Related Works

2.1. 3D-aware Video Diffusion Models

The remarkable success of diffusion models in image synthesis [22, 26, 45, 46] has been rapidly extended to the temporal domain of video generation. Foundational text-to-video models such as Video Diffusion Models [23] and Make-A-Video [43], along with more recent large-scale systems [18, 50, 55], have demonstrated the ability to generate high-fidelity and temporally coherent video clips from textual descriptions. However, precise control over the camera viewpoint remains a key challenge. To address this, one line of work [56] leverages explicit geometric condition to guide generation. Another line of methods [47, 62] learns to interpret camera parameters directly, bypassing the need for an intermediate 3D representation. The development of these controllable models provides powerful, off-the-shelf tools for generating visually consistent, multi-view data [1, 51]. In this paper, we investigate how the rich, 3D-aware priors embedded in these models can be directly harnessed to improve the performance of downstream perception tasks.

2.2. Generative Data augmentation

Before the advent of generative models, sophisticated data augmentation methods were proposed to synthesize new images [57, 58, 61]. With the recent blossoming of gener-

ative models—renowned for producing high-quality, high-fidelity, and diverse outputs—a growing number of methods now leverage them for data augmentation [13, 21, 48, 49, 63]. For instance, He et al. [21] extensively study how synthetic images from text-to-image models can be used for image recognition. Trabucco et al. [48] edit image semantics with an off-the-shelf diffusion model to generalize from few-shot examples, while Fang et al. [13] use visual priors to guide generation and employ category-calibrated CLIP scores for post-filtering.

These works primarily focus on diversifying the visual appearance of existing images. In contrast, our method leverages the temporal and spatial priors learned by video diffusion models to expand the scene spatially by generating new viewpoints and temporally by converting the static image into a dynamic video. Furthermore, to obtain reliable annotations for training an object detector, previous approaches either perform location-invariant augmentations [48] or generate objects conditioned on given bounding boxes [49, 63]. Our method, however, generates consecutive video frames and employs a foundation model [38] for automatic annotation, thereby allowing for greater flexibility in the location of the target objects.

2.3. UAV-based Object Detection

Object detection from Unmanned Aerial Vehicles (UAVs) introduces unique challenges not present in ground-based detection [2, 3, 12, 24, 52, 64]. Key research challenges in this domain stem from the nature of aerial imagery. Objects frequently appear at small scales, in dense clusters, or are sparsely distributed, requiring specialized architectures that fuse multi-resolution features [34, 35] or employ cluster-based proposal mechanisms [54]. Furthermore, constant variations in UAV altitude and viewing angles create significant appearance shifts.

For practical deployment, computational efficiency is paramount for on-board processing. This has driven a shift from slower two-stage methods towards efficient one-stage detectors, represented by YOLO [25, 39]. Recently, transformer-based DETR models have also emerged as a powerful family of object detectors [7, 59]. These models offer a favorable balance of speed and accuracy, making them a common choice for UAV-based detection systems [33].

3. Methods

In this section, we first formalize our problem and introduce our generative spatiotemporal augmentation pipeline. We then analyze how the proposed augmentation expands data coverage, followed by implementation details on annotation transfer and disocclusion handling.

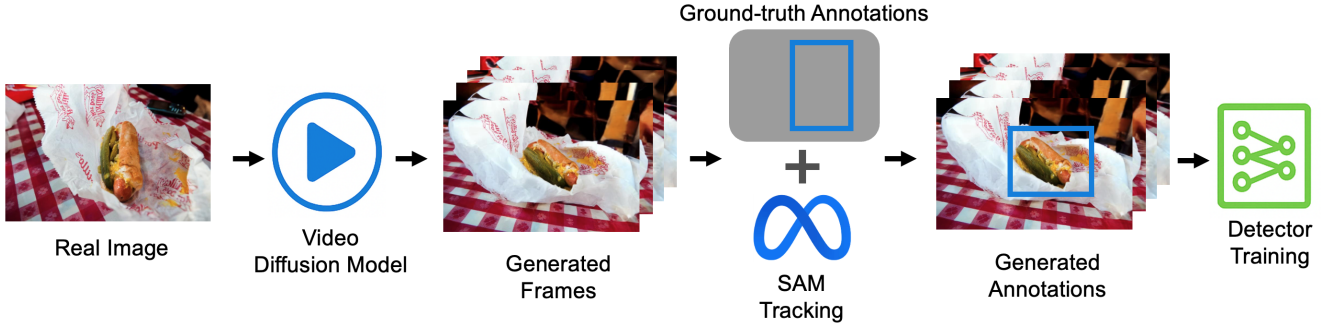


Figure 2. We use video diffusion models to expand spatially and temporally to the current scene. Thanks to the consecutive frames of the generated video, SAM 2 video segmentation model can be used to robustly, accurately and automatically generate segmentation masks and the bounding boxes for the generated frames.

3.1. Generative Spatiotemporal Augmentation

We aim to enrich training data by generating new views and dynamics from existing images using a pre-trained image-to-video diffusion model \mathcal{G} . For each original image $I_0^{(i)}$ in the dataset $\mathcal{D}_{\text{orig}}$, we generate a video sequence $\{I_t^{(i)}\}_{t=1}^T$ that depicts alternative viewpoints or motions of the same scene. By conducting this augmentation to all N images, we obtain the synthetic dataset $\mathcal{D}_{\text{new}} = \{\{I_t^{(i)}\}_{t=1}^T\}_{i=1}^N$, and the final augmented dataset $\mathcal{D}_{\text{aug}} = \mathcal{D}_{\text{orig}} \cup \mathcal{D}_{\text{new}}$.

3D Novel-View Augmentation To simulate multi-view geometry, we synthesize novel camera viewpoints of a (quasi-)static scene. Let the camera trajectory be a sequence of poses $C = \{c_t\}_{t=1}^T$, where each $c_t \in SE(3)$ specifies the rotation and translation relative to the initial view. The video model \mathcal{G} generates frames as

$$\{I_t\}_{t=1}^T = \mathcal{G}(I_0, C).$$

We then select a subset of frames indexed by $S \subseteq \{1, \dots, T\}$, $|S| = K$, to form

$$\mathcal{D}_{\text{new}} = \{I_t \mid t \in S\}.$$

This turns a single 2D image into geometrically diverse views guided by the 3D priors of \mathcal{G} .

Temporal-Dynamics Augmentation To further diversify temporal patterns, we prompt \mathcal{G} to synthesize dynamic scene evolution:

$$\{I_t\}_{t=1}^T = \mathcal{G}(I_0; \tau),$$

where τ is a temporal control signal (e.g., motion strength or duration). We sub-select frames $S \subseteq \{1, \dots, T\}$ to augment $\mathcal{D}_{\text{orig}}$, yielding \mathcal{D}_{aug} . We evaluate different video diffusion backbones, spatial cropping schemes, and frame-selection strategies to maximize augmentation utility while avoiding degenerate samples.

3.2. Coverage Expansion Analysis

Our central hypothesis is that generative spatiotemporal augmentation expands the effective coverage of a limited training set over the unseen target distribution. Unlike classical flips or crops, which perturb images locally, our method explores underrepresented axes of variation—multi-view geometry and temporal dynamics—thus enriching the data manifold along directions that standard augmentations neglect.

Quantifying Coverage. We adopt the precision–recall framework for generative models [29] to measure how an augmented training set D spans a held-out validation set U . Given a feature encoder $\phi(\cdot)$ and distance metric $d(\cdot, \cdot)$, recall is defined as

$$f(I, D) = \begin{cases} 1, & \text{if } \exists I' \in D \text{ s.t. } d(\phi(I), \phi(I')) \leq r(I', D), \\ 0, & \text{otherwise,} \end{cases} \quad (1)$$

where $r(I', D)$ is the distance to the k -th nearest neighbor of I' within D . The overall recall is

$$\text{Recall}(U \rightarrow D) = \frac{1}{|U|} \sum_{I \in U} f(I, D), \quad (2)$$

representing the fraction of validation samples whose features are covered by the training set. Following [29], we use a pretrained VGG-16 [42] with $k = 3$ for all measurements.

Coverage Growth and Diminishing Returns. As the number of synthetic frames increases, both image- and object-level recall rise sharply, confirming that the generated samples fill underrepresented regions of the data manifold. The recall curve typically saturates near 0.93 after approximately 30 frames, indicating that our augmentation

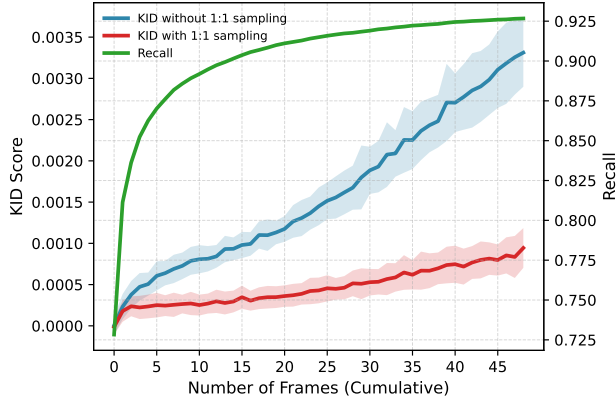


Figure 3. **Object recall and KID vs. number of synthetic frames.** Recall increases sharply then saturates after ~ 30 frames, showing diminishing returns in coverage. KID increases with frame count, but 1:1 sampling (red) stabilizes realism compared to unrestricted sampling (blue).

efficiently reaches the dominant modes of variation without excessive sampling.

Coverage–Fidelity Trade-off. Because video diffusion models produce temporally correlated frames, precision metrics are less informative. We therefore use the Kernel Inception Distance (KID) [4] to quantify the distribution shift in the training data. As shown in Fig. 3, recall improves steadily as KID increases mildly, revealing a coverage–fidelity trade-off. A 1:1 sampling ratio between real and generated images achieves the best balance, expanding coverage substantially while maintaining overall realism. Tab. 1 further confirms this Recall-KID tradeoff across different augmentation methods.

Complementarity with Existing Augmentations. While our method alone outperforms appearance-based augmentations such as Instagen [14] and ControlAug [13] in terms of coverage (Tab. 1), the largest performance gains occur when spatiotemporal and existing augmentations are combined. This suggests that our approach expands the training distribution along axes that prior methods underexplore. Moreover, in compute- or data-limited settings, the coverage efficiency of our augmentation offers a practical way to achieve diversity without retraining or extensive manual tuning.

3.3. Annotation Transfer via Video Segmentation

To use the synthetic images S for training an object detector, we require bounding-box annotations for each frame. Manually labeling these frames is prohibitively expensive, so we adopt an automated annotation pipeline.

Let B_0^j denote the ground-truth bounding box for object j in the original image I_0 . We employ a state-of-the-art

Table 1. Comparison of image and object recall under different augmentations. Results are computed using 8 generated images per original image with a 1:1 sampling ratio for all augmentation methods.

Augmentation	Raw	Instagen	ControlAug	Ours
Image Recall	88.60	97.14	98.62	98.98
Object Recall	72.83	78.42	86.46	88.56
KID \downarrow	5×10^{-6}	5.5×10^{-3}	8.7×10^{-4}	6.5×10^{-4}

video instance segmentation model \mathcal{M}_{seg} (e.g., SAM 2 [38] tracking), which tracks and segments objects throughout a video given an initial prompt. Given the generated video $V = \{I_t\}_{t=1}^T$ and the initial box B_0^j , the model produces a sequence of binary masks,

$$\{M_t^j\}_{t=1}^T = \mathcal{M}_{\text{seg}}(V, B_0^j),$$

where M_t^j is the segmentation mask for object j in frame I_t . From each mask, we compute the tightest enclosing axis-aligned bounding box,

$$B_t^j = \text{BoundingBox}(M_t^j),$$

which serves as the annotation for the corresponding synthetic image. This process is applied to all objects in I_0 , yielding a complete set of annotations for the entire generated sequence. Fig. 1 and 2 show examples and a description of this process.

3.4. Handling Disocclusion

A practical challenge in our spatiotemporal augmentation is *disocclusion*—as the virtual camera moves, regions that were previously hidden in the original image become newly visible. Because these areas have no corresponding ground-truth annotations, directly using them for training can introduce false negatives and slightly degrade detector performance. An example is shown in Fig. 4, where newly revealed background and object regions appear in the augmented view.

Tracking-Based Masking. One way to handle disocclusion is to identify and mask out the newly visible regions. We sample a uniform grid of points $P_0 = \{p_i^0\}_{i=1}^N$ on the original image I_0 and track them across generated frames using a point tracker \mathcal{T}_p (e.g. TAPNext [60] and All-Tracker [19]):

$$P_t = \{p_i^t\}_{i=1}^N = \mathcal{T}_p(V, P_0).$$

The tracked points define the visible region in each frame I_t . Masks can be generated via two ways. **a)** a polygonal boundary Ω_t constructed from the points with largest/smallest x/y coordinates yields a binary mask M_{valid}^t .

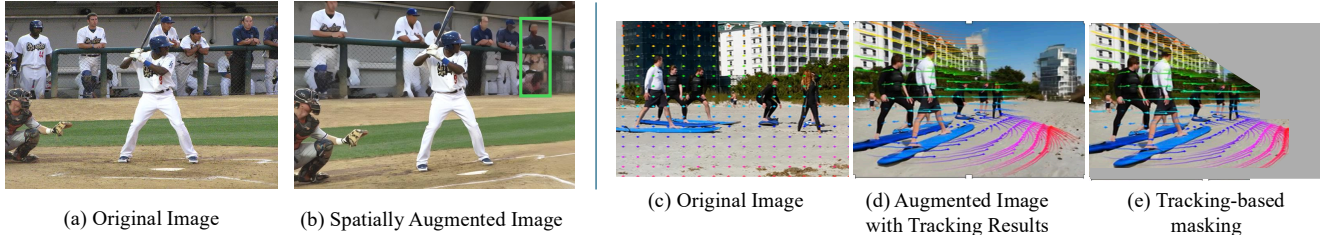


Figure 4. **Mitigating disocclusion during viewpoint changes.** (a) Original image. (b) Spatially augmented image showing newly visible regions (pseudo-label example). (c–e) Illustration of tracking-based masking: (c) original frame with grid points, (d) augmented frame with tracked points, and (e) masked result excluding disoccluded areas. These visualizations highlight that disoccluded regions can be detected and masked, though the overall performance benefit is marginal.

b) a dense point tracker can be applied to estimate correspondences for every pixel in the original image; smoothing the resulting correspondence map with a Gaussian filter and thresholding it produces a binary, pixel-wise validity mask. We then remove disoccluded pixels as

$$I'_t = I_t \odot M_{\text{valid}}^t.$$

This approach effectively suppresses unlabeled regions while preserving annotated content, as shown in Fig. 4(e).

Pseudo-Labeling Newly Visible Areas. Alternatively, we apply a simple two-pass pseudo-labeling scheme. A detector trained without masking first generates predictions for disoccluded regions, and these pseudo-labels are then incorporated in a second round of training (Fig. 4(b)). This recovers some useful supervision but adds only modest gains, as seen quantitatively in Tab. 4.

Practical Recommendation. In practice, both masking and pseudo-labeling yield only marginal improvements—typically under one mAP point (Tab. 5,4). Unless maximizing every fraction of performance, disocclusion can be safely ignored: its impact is minor compared to the overall benefits of spatiotemporal augmentation, and handling it adds extra complexity with limited return.

3.5. Choosing an Effective Configuration

Our spatiotemporal augmentation framework exposes several controllable factors for the final performance. The most important include: (1) the augmentation type (3D novel views or temporal dynamics), (2) the camera trajectory and number of generated frames, (3) frame filtering strategies, and (4) treatment of disoccluded regions (Sec. 3.4).

Guided by the Recall–KID analysis (Sec. 3.2), we find that effective configurations expand coverage while preserving perceptual fidelity. In practice, a 1:1 ratio between real and generated images, modest camera motion, and CLIP-filtered frames provide a good balance between

realism and diversity. Disocclusion handling yields only marginal benefits and can typically be ignored.

Comprehensive ablations in Sec. 4 confirm and provides further details of the controllable factors. Overall, combining existing appearance-based augmentations with our spatiotemporal method delivers the best performance, as they enrich data coverage along complementary axes.

4. Experiments

We evaluate spatiotemporal augmentation across several dimensions and evaluate using three datasets including COCO [32], VisDrone [6] and Semantic Drone [9]. We first compare against traditional baseline and other generative augmentation methods (see Fig. 5). We then analyze the interactions between augmentation types (spatial trajectories vs. temporal dynamics) and dataset characteristics, the impact of disocclusion handling strategies, and the scaling of benefits with dataset size.

4.1. Spatiotemporal Augmentation Improves Performance

A central question is whether the additional coverage provided by spatiotemporal augmentation, as shown in Sec. 3.2, translates into measurable detection gains. We therefore evaluate on COCO5k (a subset of COCO containing 5k samples) and VisDrone (6,471 training images). For COCO, we use DimensionX [47] as our video diffusion model; For VisDrone, we use LTX-Video-13B [18] with randomly cropped regions of the original images as conditioning inputs. Because aerial images contain many small objects, cropping improves generation quality. From each image, we extract 5 random crops and generate a short video clip for each. We then sample 8 frames per clip, producing 40 augmented images per original image.

We compare our spatiotemporal augmentation against both traditional geometric augmentation and recent generative augmentation baselines InstaGen [14] and ControlAug [13]. For fairness, we fix the number of generated samples across all methods, using 8 augmented images per



Figure 5. **Qualitative comparison of our spatiotemporal augmentation** on COCO and VisDrone against baselines. Our method produces video frames conditioned on the input image, yielding coherent and expressive spatial (top row) and temporal (bottom row) variation compared to the conventional geometric augmentation. ControlAug [13] synthesizes images conditioned on the HED boundary map of the original image, preserving spatial structure but altering appearance. Instagen [14] samples new images using a finetuned diffusion model guided by text prompts (e.g., “a photograph of person and bench,” or “a drone photograph containing car, pedestrian, and bicycle”).

original image. For InstaGen, annotations for synthetic images are produced using a detector pretrained on the corresponding raw dataset. For ControlAug, we generate 27 images per original sample and keep the top eight according to the CLIP-based filtering protocol proposed in the original work, corresponding to a filtering ratio of 0.3.

Table 2 reports mAP scores. On COCO5k, by combining our method with traditional augmentation, we can achieve a 3.8 point gain in mAP@50:95. Our method also achieves larger gains at stricter IoU thresholds compared to both baselines.

On VisDrone, a UAV-captured dataset characterized by viewpoint variation and limited data, the improvements are also significant. When fixing the number of augmented frames to 8x, our method also shows better performance than both baselines. Also, as a complementary dimension to appearance-based augmentation methods, combining spatiotemporal and appearance-based methods leads to further performance improvements when the amount of added data is fixed.

4.2. Results on Semantic Drone Dataset

We evaluate our approach on the Semantic Drone dataset [9] for UAV-view person detection task. This dataset consists of 400 high-resolution images captured from a nadir (bird’s-eye) view. To construct our augmented dataset, we randomly crop 10 sub-images from each original image to generate 10 short video clips with an image-conditioned video diffusion model LTX-Video-13B [18]. We sample 8 frames per video clip (selecting one frame every five frames), yielding 80 augmented images per original image. During training, we maintain the 1:1 sampling ratio between raw and augmented samples as in COCO experiments. The dataset

contains 400 images. We train the YOLO11x model on subsets of it containing 100 and 200 training samples, respectively, and use the remaining 200 images for validation. As shown in Table 3, our method consistently outperforms the baseline method with only traditional augmentation.

4.3. Experiments on Disocclusion Handling

Viewpoint changes introduce disocclusions, where newly revealed areas that may contain unlabeled objects. We explore two approaches to mitigate the resulting supervision gap: masking newly generated regions and generating pseudo-labels for objects appearing in those regions.

Masking disoccluded regions We compare three strategies for handling these regions: (i) *w/o masking* (use frames as-is), (ii) *polygon masking* that preserves the tracked, original field-of-view while discarding newly revealed areas, and (iii) *pixel-wise masking* (dense, pixel-level masking of all disoccluded pixels). As shown in Table 5, neither of the two masking strategies improves detection performance, and both even reduce accuracy on COCO5k.

We find that this degradation occurs partly because viewpoint changes in some generated frames reveal previously occluded portions of labeled objects. These objects will be partially masked, making it difficult for the model to learn accurate localization. Meanwhile, the masks produced by SAM 2 naturally extend into newly visible (disoccluded) regions, accurately capturing the full boundary of the object in these frames. Because masking out such regions would discard useful visual information, we omit disocclusion masking from our final augmentation pipeline.

Table 2. **Augmentation Effectiveness Comparison.** We compare our method against traditional augmentations, InstaGen [14], and ControlAug [13] on COCO5k and VisDrone, using the same number of generated frames (8× the original dataset size). Overall, our method outperforms the baselines, but the strongest performance is achieved when combining multiple augmentation methods.

Dataset	Method	mAP@50	mAP@50:95
COCO5k	Trad Aug	36.3	24.8
	Trad Aug + ControlAug (8x)	40.1 (+3.8)	27.6(+2.8)
	Trad Aug + InstaGen (8x)	40.3 (+4.0)	28.1(+3.3)
	Trad Aug + Ours (8x)	41.1 (+4.8)	28.6(+3.8)
	Trad Aug + Ours (4x) + ControlAug (4x)	42.6 (+6.3)	29.7(+4.9)
	Trad Aug + Ours (4x) + InstaGen (4x)	41.8 (+5.4)	29.1(+4.3)
Visdrone	Trad Aug	45.9	28.5
	Trad Aug + ControlAug (8x)	48.5 (+2.6)	30.5 (+2.0)
	Trad Aug + InstaGen (8x)	47.7 (+1.8)	29.8 (+1.3)
	Trad Aug + Ours (8x)	48.9 (+3.0)	30.7 (+2.2)
	Trad Aug + Ours (4x) + ControlAug (4x)	49.1 (+3.2)	30.8 (+2.3)
	Trad Aug + Ours (4x) + InstaGen (4x)	48.9 (+3.0)	30.8 (+2.3)
	Trad Aug + Ours (40x)	49.6 (+3.7)	31.3 (+2.8)

Table 3. Comparison of mAP on subsets of **Semantic Drone** [9]. We evaluate YOLO11x detectors trained with and without augmented data using our method on subsets size of 100 and 200 respectively.

Training set size	Augmented	mAP@50	mAP@50:95
100		71.8	39.7
100	✓	75.7 (+3.9)	44.4 (+4.7)
200		83.2	51.8
200	✓	87.4 (+4.2)	57.7 (+5.9)

Table 4. **Effect of confidence threshold on pseudo-label** to performance on COCO5k.

Conf thr.	0.5	0.6	0.7	0.8	w/o pseudo-labels
mAP@50	41.1	40.7	41.4	40.7	41.1
mAP@50:95	28.7	28.3	28.9	28.3	28.6

Pseudo-labeling We apply a simple two-pass pseudo-labeling scheme. We first train a detector on the augmented dataset without masking, then run inference on the training set and retain predictions above a specified confidence threshold that fall within the newly generated regions. These predictions serve as pseudo-labels for a second round of training. As shown in Table 4, a confidence threshold of 0.7 yields a modest improvement of 0.3 mAP@50:95.

4.4. Effects of Types of Spatiotemporal Augmentation

The most effective augmentation strategy depends on the dataset’s characteristics, as shown in Table 6.

For COCO5k, which is object-centric and often static, spatial augmentation with orbital camera trajectories perform the best. This approach exposes novel perspectives

Table 5. **Ablation on disocclusion masking.** We compare object detection performance with and without polygon and pixel-wise masking on COCO5k and VisDrone datasets.

Dataset	Method	mAP@50	mAP@50:95
COCO5k	w/o masking	41.1	28.6
	polygon masking	40.4	28.0
	pixel-wise masking	39.6	27.4
VisDrone	w/o masking	49.6	31.3
	polygon masking	49.6	31.3
	pixel-wise masking	49.5	31.1

that align with the dataset’s underlying distribution, improving recall and accuracy.

In contrast, Visdrone scenes are not object-centric, so 3D camera trajectories appear unrealistic. Here, temporal augmentation with scene dynamics is more effective. By varying object poses and scene states from similar viewpoints, this strategy enriches the dataset with in-distribution temporal variations, boosting recall without sacrificing realism.

These findings show that augmentation must match the dataset’s dominant source of variation. Spatial generation directly creates new viewpoints, while temporal generation implicitly provides new information through object motion.

Table 6. **Effects of Spatial vs. Temporal augmentation** on COCO5k and VisDrone performance. We use DimensionX [47] for spatial generation and LTX-Video-13B [18] for temporal generation.

Dataset	Method	mAP@50	mAP@50:95
COCO5k	Spatial	41.1	28.6
	Temporal	38.3	26.3
VisDrone	Spatial	49.2	31.1
	Temporal	49.6	31.3

Table 7. **Dataset Size.** Comparison of mAP for YOLO11x trained on raw vs. augmented data as training set size increases.

Dataset size	5k	10k	15k	20k	25k	30k	35k
Raw	24.8	32.9	37.0	39.4	41.7	43.2	44.6
Augmented	28.6	35.1	39.1	41.5	43.6	44.9	46.0

4.5. Performance Scaling with Dataset Size

We next study how the benefits of spatiotemporal augmentation scale with dataset size. Figure 6 plots detection performance as a function of training set size, comparing traditional augmentation and our method. YOLO11x model exhibits a large performance gap that persists even at larger dataset sizes, indicating that it can exploit the additional coverage provided by spatiotemporal augmentation. For VisDrone, where the dataset is limited to 6,471 images, we observe a $\sim 5\%$ improvement from our augmentation. This highlights that in low-data regimes, and particularly in UAV scenarios, spatiotemporal augmentation is especially valuable. Together, these results suggest that our method is most impactful when dataset characteristics allow the model to leverage the expanded coverage it provides. In addition, our spatiotemporal augmentation can be applied to detectors with different architectures. We include more discussion in the supplementary materials.

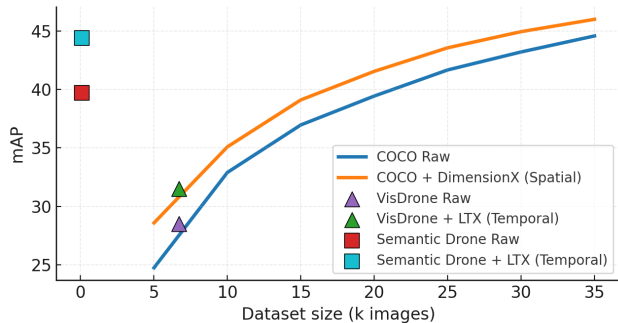


Figure 6. **Dataset size vs. mAP on 3 datasets.** Detection results of YOLOv11x on COCO under different dataset sizes

4.6. Ablation Studies

We performed ablation studies on COCO5k to optimize our method’s components: frame sampling, data ratios, pseudo-labeling, and data filtering.

Effect of Frame Sampling and Data Ratio As shown in Tables 8 and 9, training on raw data yields a 36.3 mAP@50 baseline. We found the optimal strategy is to enforce a 1:1 sampling ratio between real and synthetic data and to sparsely sample 8 frames (e.g. sample every 5 frames). This configuration achieves 41.1 mAP@50 and 28.6 mAP@50:95, a +4.8 gain in mAP@50 over the baseline, and is used as our default.

Effect of Data Filtering Using this improved 41.1

Table 8. Comparison of mAP with and without 1:1 sampling of raw and augmented data on COCO5k.

	Raw	w/o 1:1 sampling	w/ 1:1 sampling
mAP@50	36.3	39.9 (+3.6)	41.1 (+4.8)
mAP@50:95	24.8	27.9 (+3.1)	28.6 (+3.8)

Table 9. **Effect of different frame selection strategies** on COCO5k performance. Frame selection starts from the first frame of the generated video. The 1:1 sampling ratio is employed for all experiments.

Data	#Frames per img	mAP@50	mAP@50:95
Raw	–	36.3	24.8
Sample every 3 frames	8	40.7	28.2
Sample every 4 frames	8	41.1	28.5
Sample every 5 frames	8	41.1	28.6
Use first 36 frames	36	40.5	28.3

Table 10. **CLIP-based filtering.** Performance optimization by filtering augmented data on COCO5k.

Removed samples	w/o filtering	5%	10%	20%
mAP@50	41.1	40.5	41.4	40.4
mAP@50:95	28.6	28.3	29.0	28.2

mAP@50 baseline, we further explore the effect of incorporating a CLIP-based data filtering strategy to remove low-quality generated samples. We follow the data filtering protocol as [13]. As shown in Table 10, filtering out 10% of low-quality synthetic samples gives a final slight boost to 41.4 mAP@50 and 29.0 mAP@50:95.

These ablations confirm that 1:1 sampling and sparse frame selection are crucial for achieving optimal performance, while optional data filtering can provide a marginal additional improvement. A more detailed discussion of the ablation studies is provided in the supplementary material.

5. Conclusion

We show that spatiotemporal augmentation with video diffusion models is an effective way to boost object detection in data-scarce settings. Unlike prior approaches, our method expands data along the critical axes of camera viewpoint and scene dynamics, yielding substantial gains in low-data regimes such as UAV-captured imagery. Beyond these improvements, we provide practical guidelines for implementation, including model choice, annotation transfer, and disocclusion handling. Our experiments demonstrate that this approach meaningfully broadens the training distribution and improves performance when annotated data is the bottleneck.

Acknowledgements This research was supported by the Army Research Office (ARO) under Grant No. W911NF25-1-0047.

References

- [1] Sherwin Bahmani, Ivan Skorokhodov, Guocheng Qian, Aliaksandr Siarohin, Willi Menapace, Andrea Tagliasacchi, David B Lindell, and Sergey Tulyakov. Ac3d: Analyzing and improving 3d camera control in video diffusion transformers. In *Proceedings of the Computer Vision and Pattern Recognition Conference*, pages 22875–22889, 2025. 2
- [2] Mohammadamin Barekatin, Miquel Martí, Hsueh-Fu Shih, Samuel Murray, Kotaro Nakayama, Yutaka Matsuo, and Helmut Prendinger. Okutama-action: An aerial view video dataset for concurrent human action detection. In *Proceedings of the IEEE conference on computer vision and pattern recognition workshops*, pages 28–35, 2017. 2
- [3] U Benchmark. A benchmark and simulator for uav tracking. In *European conference on computer vision*, 2016. 2
- [4] Mikołaj Bińkowski, Danica J Sutherland, Michael Arbel, and Arthur Gretton. Demystifying mmd gans. *arXiv preprint arXiv:1801.01401*, 2018. 4
- [5] Andreas Blattmann, Tim Dockhorn, Sumith Kulal, Daniel Mendelevitch, Maciej Kilian, Dominik Lorenz, Yam Levi, Zion English, Vikram Voleti, Adam Letts, et al. Stable video diffusion: Scaling latent video diffusion models to large datasets. *arXiv preprint arXiv:2311.15127*, 2023. 1
- [6] Yaru Cao, Zhijian He, Lujia Wang, Wenguan Wang, Yixuan Yuan, Dingwen Zhang, Jinglin Zhang, Pengfei Zhu, Luc Van Gool, Junwei Han, et al. Visdrone-det2021: The vision meets drone object detection challenge results. In *Proceedings of the IEEE/CVF International conference on computer vision*, pages 2847–2854, 2021. 2, 5, 1
- [7] Nicolas Carion, Francisco Massa, Gabriel Synnaeve, Nicolas Usunier, Alexander Kirillov, and Sergey Zagoruyko. End-to-end object detection with transformers. In *European conference on computer vision*, pages 213–229. Springer, 2020. 1, 2
- [8] Liang-Chieh Chen, George Papandreou, Florian Schroff, and Hartwig Adam. Rethinking atrous convolution for semantic image segmentation. *arXiv preprint arXiv:1706.05587*, 2017. 1
- [9] Ayush Dabra. drone-images-semantic-segmentation. <https://github.com/ayushdabra/drone-images-semantic-segmentation>, 2021. 2, 5, 6, 7, 1, 3
- [10] Jia Deng, Wei Dong, Richard Socher, Li-Jia Li, Kai Li, and Li Fei-Fei. Imagenet: A large-scale hierarchical image database. In *2009 IEEE conference on computer vision and pattern recognition*, pages 248–255. Ieee, 2009. 1
- [11] Alexey Dosovitskiy, Lucas Beyer, Alexander Kolesnikov, Dirk Weissenborn, Xiaohua Zhai, Thomas Unterthiner, Mostafa Dehghani, Matthias Minderer, Georg Heigold, Sylvain Gelly, et al. An image is worth 16x16 words: Transformers for image recognition at scale. *arXiv preprint arXiv:2010.11929*, 2020. 1
- [12] Dawei Du, Yuankai Qi, Hongyang Yu, Yifan Yang, Kaiwen Duan, Guorong Li, Weigang Zhang, Qingming Huang, and Qi Tian. The unmanned aerial vehicle benchmark: Object detection and tracking. In *Proceedings of the European conference on computer vision (ECCV)*, pages 370–386, 2018. 2
- [13] Haoyang Fang, Boran Han, Shuai Zhang, Su Zhou, Cuixiong Hu, and Wen-Ming Ye. Data augmentation for object detection via controllable diffusion models. In *Proceedings of the IEEE/CVF winter conference on applications of computer vision*, pages 1257–1266, 2024. 2, 4, 5, 6, 7, 8
- [14] Chengjian Feng, Yujie Zhong, Zequn Jie, Weidi Xie, and Lin Ma. Instagen: Enhancing object detection by training on synthetic dataset. In *Proceedings of the IEEE/CVF Conference on Computer Vision and Pattern Recognition*, pages 14121–14130, 2024. 4, 5, 6, 7
- [15] Ross Girshick. Fast r-cnn. In *Proceedings of the IEEE international conference on computer vision*, pages 1440–1448, 2015. 1
- [16] Ian J Goodfellow, Jean Pouget-Abadie, Mehdi Mirza, Bing Xu, David Warde-Farley, Sherjil Ozair, Aaron Courville, and Yoshua Bengio. Generative adversarial nets. *Advances in neural information processing systems*, 27, 2014. 1
- [17] Aaron Grattafiori, Abhimanyu Dubey, Abhinav Jauhri, Abhinav Pandey, Abhishek Kadian, Ahmad Al-Dahle, Aiesha Letman, Akhil Mathur, Alan Schelten, Alex Vaughan, et al. The llama 3 herd of models. *arXiv preprint arXiv:2407.21783*, 2024. 1
- [18] Yoav HaCohen, Nisan Chiprut, Benny Brazowski, Daniel Shalem, Dudu Moshe, Eitan Richardson, Eran Levin, Guy Shiran, Nir Zabari, Ori Gordon, et al. Ltx-video: Realtime video latent diffusion. *arXiv preprint arXiv:2501.00103*, 2024. 1, 2, 5, 6, 7
- [19] Adam W Harley, Yang You, Xinglong Sun, Yang Zheng, Nikhil Raghuraman, Yunqi Gu, Sheldon Liang, Wen-Hsuan Chu, Achal Dave, Suyu You, et al. Alltracker: Efficient dense point tracking at high resolution. In *Proceedings of the IEEE/CVF International Conference on Computer Vision*, pages 5253–5262, 2025. 4, 2
- [20] Kaiming He, Xiangyu Zhang, Shaoqing Ren, and Jian Sun. Deep residual learning for image recognition. In *Proceedings of the IEEE conference on computer vision and pattern recognition*, pages 770–778, 2016. 1
- [21] Ruifei He, Shuyang Sun, Xin Yu, Chuhui Xue, Wenqing Zhang, Philip Torr, Song Bai, and Xiaojuan Qi. Is synthetic data from generative models ready for image recognition? *arXiv preprint arXiv:2210.07574*, 2022. 2
- [22] Jonathan Ho, Ajay Jain, and Pieter Abbeel. Denoising diffusion probabilistic models. *Advances in neural information processing systems*, 33:6840–6851, 2020. 1, 2
- [23] Jonathan Ho, Tim Salimans, Alexey Gritsenko, William Chan, Mohammad Norouzi, and David J Fleet. Video diffusion models. *Advances in neural information processing systems*, 35:8633–8646, 2022. 2
- [24] Meng-Ru Hsieh, Yen-Liang Lin, and Winston H Hsu. Drone-based object counting by spatially regularized regional proposal network. In *Proceedings of the IEEE international conference on computer vision*, pages 4145–4153, 2017. 2
- [25] Glenn Jocher and Jing Qiu. Ultralytics yolo11, 2024. 2, 3
- [26] Tero Karras, Miika Aittala, Timo Aila, and Samuli Laine. Elucidating the design space of diffusion-based generative

- models. *Advances in neural information processing systems*, 35:26565–26577, 2022. 2
- [27] Alexander Kirillov, Eric Mintun, Nikhila Ravi, Hanzi Mao, Chloe Rolland, Laura Gustafson, Tete Xiao, Spencer Whitehead, Alexander C Berg, Wan-Yen Lo, et al. Segment anything. In *Proceedings of the IEEE/CVF international conference on computer vision*, pages 4015–4026, 2023. 1, 2
- [28] Alex Krizhevsky, Ilya Sutskever, and Geoffrey E Hinton. Imagenet classification with deep convolutional neural networks. *Advances in neural information processing systems*, 25, 2012. 1
- [29] Tuomas Kynkäänniemi, Tero Karras, Samuli Laine, Jaakko Lehtinen, and Timo Aila. Improved precision and recall metric for assessing generative models. *Advances in neural information processing systems*, 32, 2019. 3
- [30] Junnan Li, Dongxu Li, Silvio Savarese, and Steven Hoi. Blip-2: Bootstrapping language-image pre-training with frozen image encoders and large language models. In *International conference on machine learning*, pages 19730–19742. PMLR, 2023. 1
- [31] Yanghao Li, Hanzi Mao, Ross Girshick, and Kaiming He. Exploring plain vision transformer backbones for object detection. In *European conference on computer vision*, pages 280–296. Springer, 2022. 1
- [32] Tsung-Yi Lin, Michael Maire, Serge Belongie, James Hays, Pietro Perona, Deva Ramanan, Piotr Dollár, and C Lawrence Zitnick. Microsoft coco: Common objects in context. In *European conference on computer vision*, pages 740–755. Springer, 2014. 1, 2, 5
- [33] Mingjie Liu, Xianhao Wang, Anjian Zhou, Xiuyuan Fu, Yiwei Ma, and Changhao Piao. Uav-yolo: Small object detection on unmanned aerial vehicle perspective. *Sensors*, 20(8): 2238, 2020. 2
- [34] Yingjie Liu, Fengbao Yang, and Peng Hu. Small-object detection in uav-captured images via multi-branch parallel feature pyramid networks. *IEEE access*, 8:145740–145750, 2020. 2
- [35] Ziming Liu, Guangyu Gao, Lin Sun, and Zhiyuan Fang. Hrdnet: High-resolution detection network for small objects. *arXiv preprint arXiv:2006.07607*, 2020. 2
- [36] Aaron van den Oord, Nal Kalchbrenner, and Koray Kavukcuoglu. Pixel recurrent neural networks. *arXiv preprint arXiv:1601.06759*, 2016. 1
- [37] Ben Poole, Ajay Jain, Jonathan T Barron, and Ben Mildenhall. Dreamfusion: Text-to-3d using 2d diffusion. *arXiv preprint arXiv:2209.14988*, 2022. 1
- [38] Nikhila Ravi, Valentin Gabeur, Yuan-Ting Hu, Ronghang Hu, Chaitanya Ryali, Tengyu Ma, Haitham Khedr, Roman Rädle, Chloe Rolland, Laura Gustafson, et al. Sam 2: Segment anything in images and videos. *arXiv preprint arXiv:2408.00714*, 2024. 2, 4
- [39] Joseph Redmon, Santosh Divvala, Ross Girshick, and Ali Farhadi. You only look once: Unified, real-time object detection. In *Proceedings of the IEEE conference on computer vision and pattern recognition*, pages 779–788, 2016. 1, 2
- [40] Robin Rombach, Andreas Blattmann, Dominik Lorenz, Patrick Esser, and Björn Ommer. High-resolution image synthesis with latent diffusion models. In *Proceedings of the IEEE/CVF conference on computer vision and pattern recognition*, pages 10684–10695, 2022. 1
- [41] Olaf Ronneberger, Philipp Fischer, and Thomas Brox. U-net: Convolutional networks for biomedical image segmentation. In *International Conference on Medical image computing and computer-assisted intervention*, pages 234–241. Springer, 2015. 1
- [42] Karen Simonyan and Andrew Zisserman. Very deep convolutional networks for large-scale image recognition. *arXiv preprint arXiv:1409.1556*, 2014. 3
- [43] Uriel Singer, Adam Polyak, Thomas Hayes, Xi Yin, Jie An, Songyang Zhang, Qiyuan Hu, Harry Yang, Oron Ashual, Oran Gafni, et al. Make-a-video: Text-to-video generation without text-video data. *arXiv preprint arXiv:2209.14792*, 2022. 2
- [44] Shweta Singh, Aayan Yadav, Jitesh Jain, Humphrey Shi, Justin Johnson, and Karan Desai. Benchmarking object detectors with coco: A new path forward. In *European Conference on Computer Vision*, pages 279–295. Springer, 2024. 1
- [45] Jiaming Song, Chenlin Meng, and Stefano Ermon. Denoising diffusion implicit models. *arXiv preprint arXiv:2010.02502*, 2020. 2
- [46] Yang Song, Jascha Sohl-Dickstein, Diederik P Kingma, Abhishek Kumar, Stefano Ermon, and Ben Poole. Score-based generative modeling through stochastic differential equations. *arXiv preprint arXiv:2011.13456*, 2020. 2
- [47] Wenqiang Sun, Shuo Chen, Fangfu Liu, Zilong Chen, Yueqi Duan, Jun Zhang, and Yikai Wang. Dimensionx: Create any 3d and 4d scenes from a single image with controllable video diffusion. *arXiv preprint arXiv:2411.04928*, 2024. 1, 2, 5, 7
- [48] Brandon Trabucco, Kyle Doherty, Max Gurinas, and Ruslan Salakhutdinov. Effective data augmentation with diffusion models. *arXiv preprint arXiv:2302.07944*, 2023. 2
- [49] Anh-Khoa Nguyen Vu, Quoc-Truong Truong, Vinh-Tiep Nguyen, Thanh Duc Ngo, Thanh-Toan Do, and Tam V Nguyen. Multi-perspective data augmentation for few-shot object detection. *arXiv preprint arXiv:2502.18195*, 2025. 2
- [50] Team Wan, Ang Wang, Baole Ai, Bin Wen, Chaojie Mao, Chen-Wei Xie, Di Chen, Feiwu Yu, Haiming Zhao, Jianxiao Yang, et al. Wan: Open and advanced large-scale video generative models. *arXiv preprint arXiv:2503.20314*, 2025. 2
- [51] Rundi Wu, Ruiqi Gao, Ben Poole, Alex Trevithick, Changxi Zheng, Jonathan T Barron, and Aleksander Holynski. Cat4d: Create anything in 4d with multi-view video diffusion models. In *Proceedings of the Computer Vision and Pattern Recognition Conference*, pages 26057–26068, 2025. 2
- [52] Zhenyu Wu, Karthik Suresh, Priya Narayanan, Hongyu Xu, Heesung Kwon, and Zhangyang Wang. Delving into robust object detection from unmanned aerial vehicles: A deep nuisance disentanglement approach. In *Proceedings of the IEEE/CVF international conference on computer vision*, pages 1201–1210, 2019. 2
- [53] Bin Xiao, Haiping Wu, Weijian Xu, Xiyang Dai, Houdong Hu, Yumao Lu, Michael Zeng, Ce Liu, and Lu Yuan.

- Florence-2: Advancing a unified representation for a variety of vision tasks. In *Proceedings of the IEEE/CVF Conference on Computer Vision and Pattern Recognition*, pages 4818–4829, 2024. 1
- [54] Fan Yang, Heng Fan, Peng Chu, Erik Blasch, and Haibin Ling. Clustered object detection in aerial images. In *Proceedings of the IEEE/CVF international conference on computer vision*, pages 8311–8320, 2019. 2
- [55] Zhuoyi Yang, Jiayan Teng, Wendi Zheng, Ming Ding, Shiyu Huang, Jiazheng Xu, Yuanming Yang, Wenyi Hong, Xiaohan Zhang, Guanyu Feng, et al. Cogvideox: Text-to-video diffusion models with an expert transformer. *arXiv preprint arXiv:2408.06072*, 2024. 2
- [56] Wangbo Yu, Jinbo Xing, Li Yuan, Wenbo Hu, Xiaoyu Li, Zhipeng Huang, Xiangjun Gao, Tien-Tsin Wong, Ying Shan, and Yonghong Tian. Viewcrafter: Taming video diffusion models for high-fidelity novel view synthesis. *arXiv preprint arXiv:2409.02048*, 2024. 1, 2
- [57] Sangdoon Yun, Dongyoon Han, Seong Joon Oh, Sanghyuk Chun, Junsuk Choe, and Youngjoon Yoo. Cutmix: Regularization strategy to train strong classifiers with localizable features. In *Proceedings of the IEEE/CVF international conference on computer vision*, pages 6023–6032, 2019. 2
- [58] Hongyi Zhang, Moustapha Cisse, Yann N Dauphin, and David Lopez-Paz. mixup: Beyond empirical risk minimization. *arXiv preprint arXiv:1710.09412*, 2017. 2
- [59] Yian Zhao, Wenyu Lv, Shangliang Xu, Jinman Wei, Guanzhong Wang, Qingqing Dang, Yi Liu, and Jie Chen. Detrs beat yolos on real-time object detection, 2023. 2
- [60] Artem Zhohus, Carl Doersch, Yi Yang, Skanda Koppula, Viorica Patraucean, Xu Owen He, Ignacio Rocco, Mehdi SM Sajjadi, Sarath Chandar, and Ross Goroshin. Tapnext: Tracking any point (tap) as next token prediction. *arXiv preprint arXiv:2504.05579*, 2025. 4, 2
- [61] Zhun Zhong, Liang Zheng, Guoliang Kang, Shaozi Li, and Yi Yang. Random erasing data augmentation. In *Proceedings of the AAAI conference on artificial intelligence*, pages 13001–13008, 2020. 2
- [62] Jensen Zhou, Hang Gao, Vikram Voleti, Aaryaman Vasishtha, Chun-Han Yao, Mark Boss, Philip Torr, Christian Rupprecht, and Varun Jampani. Stable virtual camera: Generative view synthesis with diffusion models. *arXiv preprint arXiv:2503.14489*, 2025. 1, 2
- [63] Jingyuan Zhu, Shiyu Li, Yuxuan Andy Liu, Jian Yuan, Ping Huang, Jiulong Shan, and Huimin Ma. Odgen: Domain-specific object detection data generation with diffusion models. *Advances in Neural Information Processing Systems*, 37: 63599–63633, 2024. 2
- [64] Pengfei Zhu, Longyin Wen, Dawei Du, Xiao Bian, Heng Fan, Qinghua Hu, and Haibin Ling. Detection and tracking meet drones challenge. *IEEE Transactions on Pattern Analysis and Machine Intelligence*, 44(11):7380–7399, 2021. 2

Generative Spatiotemporal Data Augmentation

Supplementary Material

6. Implementation Details

6.1. Data Generation

Spatial Video Generation For 3D spatial video generation, we use the orbital DimensionX model [47], which produces videos of a static scene with a camera moving along an orbital trajectory, conditioned on an input image and a text prompt. We obtain the text prompt using a BLIP-2-generated caption [30], and resize and crop the input image to 720×480 , the resolution required by DimensionX.

Temporal Video Generation For 3D spatial video generation, we use the image-conditioned LTX-Video-13B [18]. We generate an image caption with Florence-2-large [53] and use Llama-3.2-3B [17] to write a video prompt based on the generated caption. For COCO [32], each image is first resized using our resolution-adjustment rule: if the image area exceeds 768×576 , we uniformly downscale it so that its area matches this limit, and then round both height and width up to the nearest multiple of 32 to satisfy the model’s resolution constraints. For VisDrone [6], we extract five random 768×576 crops from each image and generate one 81-frame video clip per crop. From each clip, we sample 8 frames at 5-frame intervals, yielding 40 augmented images per original image. For Semantic Drone [9], the higher image resolution requires an additional rescaling step: we randomly rescale and crop ten 768×576 regions per image, generate one video clip for each region, and again sample 8 frames every 5 frames. This produces 80 augmented images per original image.

We use the following prompts to Llama-3.2-3B for video prompt generation on COCO and Visdrone respectively.

COCO

Instruction:

Generate a single-paragraph prompt for a video generation model based on a given caption.

Guidelines:

- **Start with a literal description** of the scene shown in the caption. This visual description is the highest priority.
- Follow with **main action or movement**, then add **specific gestures, motions, or changes over time**, if present.
- Include **details of gestures, motion, and camera behavior** (e.g., panning, zooming, circling, track-

ing).

- If the caption describes a static scene (e.g., no people or actions), add **camera movement** (e.g., slow pan, orbit, dolly) to bring the scene to life. Do **not** simply restate the caption.
- **Do not introduce any new people, objects, or elements** not present in the caption. If the caption has no people, do not describe human actions.
- The entire prompt must be **under 100 words**.
- Use **precise, chronological, and detailed** descriptions.
- **Output only the generated prompt.**

Visdrone

Instruction:

Generate a single-paragraph prompt for a video generation model based on a given caption, assuming the video is captured from a **drone’s perspective**.

Guidelines:

- **Begin with a literal and visual description** of the scene as seen from the drone. Prioritize accurate portrayal of the setting and spatial layout from above or as appropriate for a drone.
- Follow with the **main action or movement**, then describe **any dynamic elements**, such as motions, gestures, or environmental changes visible from the aerial view.
- Include **details about drone movement**—such as hovering, ascending, descending, panning, circling, tracking, or sweeping—matching the scene’s content and emphasizing temporal progression.
- If the caption depicts a **static or natural landscape**, animate the scene using **drone motion** (e.g., slow orbit, forward glide, downward tilt).
- **Do not add any elements not explicitly present** in the caption (e.g., avoid introducing people, animals, or vehicles not mentioned).
- Keep the prompt **under 100 words**, using **precise, chronological, and detailed language** suited for a drone-shot video.
- **Output only the generated prompt.**

Algorithm 1 Dense Disocclusion Mask Computation

Require: Video frames $V = \{I_1, \dots, I_T\}$; visibility threshold τ_{vis} ; confidence threshold τ_{conf} ; Gaussian std σ ; weight threshold τ_w

- 1: Convert frames to tensor of shape $(T, H, W, 3)$
- 2: Generate pixel grid $G \in \mathbb{R}^{1 \times H \times W \times 2}$
- 3: Run flow model to obtain:

$$\text{flows, visconf} \leftarrow \text{Model.forward_sliding}(V)$$

- 4: Compute pixel trajectories:

$$\text{traj_maps} = \text{flows} + G$$

- 5: Compute

$$\text{visibs} \in \{0, 1\}^{H \times W \times T}$$

using thresholds τ_{vis} and τ_{conf}

- 6: **for** $t = 1$ to T **do**

- 7: Select visible points:

$$P_t = \{(x, y) \mid \text{visibs}[t, i, j] = 1\}$$

where $(x, y) = \text{traj_maps}[t, i, j]$

- 8: Initialize impulse image $M_t \in \mathbb{R}^{H \times W}$ to zeros
- 9: For each $(x, y) \in P_t$, set $M_t[y, x] \leftarrow 1$
- 10: Construct Gaussian kernel K with radius 3σ
- 11: Compute density map:

$$W_t = \text{Conv2D}(M_t, K)$$

- 12: Threshold to obtain disocclusion mask:

$$\text{mask}_t = (W_t \geq \tau_w)$$

- 13: **end for**

- 14: **return** $\{\text{mask}_t\}_{t=1}^T$
-

6.2. Disocclusion Handling

Computing Disocclusion Masks For polygon masking, we place a 16×16 grid of points on the first frame and track them through the video using TAPNext [60]. For each generated frame, we compute the convex hull of the tracked points and mask out all pixels outside this polygon.

For dense masking, we use AllTracker [19] to track every pixel in the first frame throughout the video. For each generated frame, we compute a density map by counting tracked points in each pixel’s neighborhood, weighted by a Gaussian kernel. We obtain the disocclusion mask by thresholding this map, masking pixels whose density falls below a specified threshold, indicating newly exposed or generated regions. See Alg. 1 for details.

Pseudo-labeling For pseudo-labeling, we apply a simple two-pass pseudo-labeling scheme. We first train a detector on the augmented dataset without masking, then run inference on the training set and retain predictions that satisfy all of the following criteria:

- Confidence exceeds a specified threshold.
- The proportion of masked area (from the dense disocclusion mask) within the predicted bounding box exceeds a given ratio of the box area.
- IoU with any ground truth box (from SAM 2) is below a threshold, to avoid duplicate labels.

In our experiments, we set both the masked-area ratio threshold and the IoU threshold to 0.5.

6.3. Detector Training Settings

We utilize the YOLO11 models implemented in the Ultralytics [25] framework. The models are trained from scratch on the target dataset. All experiments are conducted with an input resolution of 640×640 pixels and a batch size of 64. We employ Stochastic Gradient Descent (SGD) as the optimizer with a momentum of 0.937 and a weight decay of 5×10^{-4} . The initial learning rate is set to $\text{lr}_0 = 0.01$ with a linear decay schedule to a final learning rate factor of $\text{lrf} = 0.01$. We train the models for 400 epochs (800 epochs for YOLO11n to ensure convergence) with a warm-up period of 3 epochs. We apply YOLO11’s standard data augmentation pipeline to all experiments, including Mosaic augmentation (probability 1.0), horizontal flipping (probability 0.5), translation ($\pm 10\%$), scaling ($\pm 50\%$), and color space augmentations in the HSV domain with hue (0.015), saturation (0.7), and value (0.4) fractions.

7. Training with RT-DETR

We also apply our method to the Transformer-based end-to-end detector, RT-DETR [59], to demonstrate that our approach generalizes well across different architectures.

We utilize the RT-DETR-x model implemented in the Ultralytics [25] framework. The model is trained from scratch without pretraining. All experiments are conducted with an input resolution of 640×640 pixels and a batch size of 64.

As shown in Figure 7 and Table 11, training with our method consistently outperforms the baseline. This confirms that our method can be robustly applied to diverse model architectures, including both CNN-based and Transformer-based models. Notably, we observe that when data is scarce (5k samples), our method outperforms the baseline by a significant margin. We hypothesize that this is due to the data-hungry nature of Transformers; therefore, generating additional data in data-scarce regimes yields a substantial boost in performance.

Table 11. Comparison of mAP@50:95 for **RT-DETR-x** trained on raw vs. augmented data as training set size increases.

Dataset size	5k	10k	15k	20k
Raw	19.8	30.0	34.1	36.1
Augmented	24.5 (+4.7)	31.7 (+1.7)	35.3 (+1.2)	38.9 (+2.8)

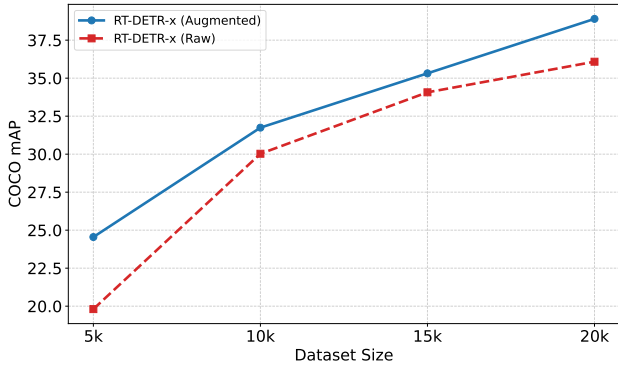


Figure 7. Detection results of RT-DETR-x on COCO under different dataset sizes

8. Additional Analyses

8.1. Effects of Model Capacity

To investigate how the effectiveness of our augmentation method scales with model capacity, we also train a smaller YOLO11n [25] on raw and augmented COCO datasets under different dataset sizes. As shown in Fig. 8, the effect depends strongly on model capacity. For the low-capacity YOLO model, the initial gap between the two augmentation strategies is small and diminishes further as training data increases, suggesting that limited-capacity models quickly saturate regardless of augmentation. In contrast, the high-capacity YOLO model exhibits a much larger performance gap that persists even at larger dataset sizes, indicating that stronger models can exploit the additional coverage provided by spatiotemporal augmentation.

Table 12. Comparison of mAP@50:95 for **YOLO11n** trained on raw vs. augmented data as training set size increases.

Dataset size	5k	10k	15k	20k	25k	30k	35k
Raw	18.7	24.2	27.5	29.8	31.2	32.7	33.6
Augmented	20.7	26.3	29.3	31.4	32.6	33.4	34.2

8.2. Performance vs Dataset Set on Semantic Drone

To investigate the effectiveness of our method on Semantic Drone [9] when more data is available, we additionally train on 300 images, and evaluate on the remaining 100 images. As shown in Tab. 13, the benefit of our augmentation

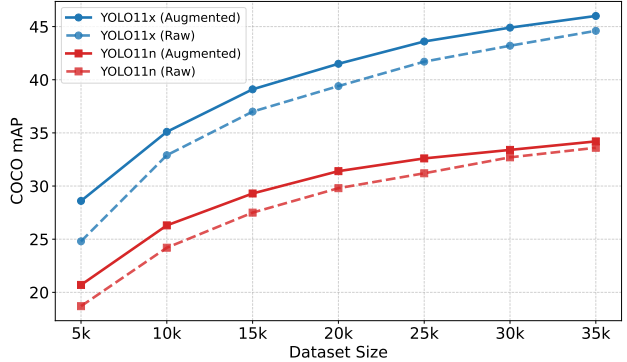


Figure 8. **Performance vs Model Capacity.** Detection results of YOLO11x and YOLO11n on COCO under different dataset sizes

diminishes at this scale. Since the task is relatively simple, the baseline model is already near saturation. Nonetheless, our spatiotemporal augmentation still yields a 2.1-point improvement in mAP@50:95.

Table 13. Comparison of mAP on subsets of **Semantic Drone** [9]. We evaluate YOLO11x detectors trained with and without augmented data using our method on subsets size of 100, 200, and 300, respectively. All models are evaluated on the remaining 100 images.

Training set size	Augmented	mAP@50	mAP@50:95
100		71.1	39.4
100	✓	74.5 (+3.4)	44.1 (+4.7)
200		81.9	51.3
200	✓	86.8 (+4.9)	56.8 (+5.5)
300		89.8	61.3
300	✓	90.7 (+0.9)	63.4 (+2.1)

8.3. Effects on Pretrained Models

Pretraining on large, diverse datasets such as COCO is a standard strategy for improving detection performance in data-scarce domains like drone datasets. Our spatiotemporal augmentation method remains effective even when applied in this pretraining–finetuning pipeline. As shown in Table 14, finetuning a COCO-pretrained YOLO11x model on VisDrone with our augmented data yields consistent gains over both the raw-data baseline and the pre-trained baseline, improving mAP@50 by 2.0 points and mAP@50:95 by 1.6 points. Although the improvements are slightly smaller than those observed when training from scratch, which reflects the strong initialization provided by COCO pretraining, the results demonstrate that our approach complements pretrained representations rather than duplicating them, providing meaningful additional signal during finetuning.

Table 14. **Effectiveness on Pretrained Models.** We finetune a COCO-pretrained YOLO11x model on Visdrone with and without our augmentation method. Our model can still improve performance significantly in the finetuning setting. Traditional augmentations are applied to all experiments.

Data	Pretrained	mAP@50	mAP@50:95
Raw		45.9	28.5
Augmented		49.6 (+3.7)	31.3 (+2.8)
Raw	✓	48.2	30.1
Augmented	✓	50.2 (+2.0)	31.7 (+1.6)

8.4. Ablation on Random Crop on Visdrone

Due to the large scene scale and small object size in aerial imagery, directly conditioning the video diffusion model on full-resolution images often leads to suboptimal synthesis quality. To address this, we provide the video diffusion model with randomly cropped regions of each image, allowing it to focus on local content. We conduct an ablation study to verify that such random cropping improves downstream detection performance.

Table 15. **Ablation on random cropping for Visdrone.** We train YOLO11x on augmented Visdrone datasets using frames from videos generated from resized full images or from randomly cropped regions, respectively. The table reports mAP@50 and mAP@50:95, showing that random cropping consistently improves detection performance, with larger numbers of crops yielding the strongest gains.

Data	mAP@50	mAP@50:95
Raw	45.9	28.5
Resize (8x)	48.2 (+2.3)	30.3 (+1.8)
Random crop (8x)	48.9 (+3.0)	30.7 (+2.2)
Random crop (40x)	49.6 (+3.7)	31.3 (+2.8)

As shown in Tab. 15, using frames generated from resized full images yields a clear improvement over training on raw data alone (+2.3 mAP@50 and +1.8 mAP@50:95). However, replacing the resized inputs with randomly cropped regions leads to consistently stronger gains under the same number of augmentation images (+3.0 and +2.2), confirming that localized conditioning produces higher-quality and more informative synthetic views. Increasing the number of random crops further amplifies this effect: using 40x augmentation (5 crops per original image) pushes performance to 49.6 mAP@50 and 31.3 mAP@50:95, corresponding to improvements of +3.7 and +2.8 over the baseline. These results demonstrate that random cropping not only enhances generative quality but also translates into tangible detector gains.

9. Limitations

While our method demonstrates superior performance across various datasets and settings, we acknowledge several limitations. First, the performance gain provided by generative data augmentation diminishes as the size of the original dataset increases. As real data covers more of the underlying distribution, the marginal benefit of synthetic data naturally declines. Second, the computational cost of video diffusion models is significant; scaling to larger datasets requires substantial computational resources. Finally, our automatic annotation pipeline relies heavily on the SAM model. Consequently, any failures or inaccuracies in SAM directly propagate to our annotation process. Addressing these constraints remains a direction for future work.